Ultrafast shift and injection currents observed in wurtzite semiconductors via emitted terahertz radiation

N. Laman, M. Bieler,[a] and H. M. van Driel[b]
Department of Physics and Institute for Optical Sciences, University of Toronto, Toronto, Canada M5S 1A7

(Received 17 June 2005; accepted 7 October 2005; published online 18 November 2005)

Shift and injection currents are generated in the wurtzite semiconductors CdSe and CdS at 295 K using above-band-gap ($\hbar\omega > E_g$) femtosecond pulses and detected via the emitted terahertz radiation; the optical beams are normally incident on samples with the optic axis in the plane of the surface. For optical intensities up to 75 MW cm^{-2} (or carrier density $<10^{18}$ cm^{-3}) the terahertz radiation amplitude shows the expected linear dependence and also varies with optical polarization and sample orientation consistent with the third-rank tensors that govern the current generation processes in the wurtzite structure. The largest shift currents are generated along the optical axis for light polarized along that axis. In CdSe with $\hbar\omega = 1.80$ eV (690 nm), the electron shift distance is ~40% of the 0.25 nm bond length and the peak current density is 5 kA cm^{-2} for an optical intensity of 10 MW cm^{-2}; for CdS the corresponding experiment at $\hbar\omega = 3.0$ eV (410 nm) gives a shift distance ~80% of the 0.26 nm bond length with a peak current density of 50 kA cm^{-2} for an incident intensity of 75 MW cm^{-2}. For injection current produced in CdSe with circularly polarized 690 nm excitation, electrons are injected with an average speed of 9 km s^{-1}; this is ~3% of the group velocity for electrons excited with the same energy. The corresponding values for CdS excited at 410 nm are 20 km s^{-1} and 2%. From the temporal characteristics of the terahertz emission for injection currents in CdS we deduce that the electron momentum scattering time is <100 fs, consistent with mobility studies. © *2005 American Institute of Physics*. [DOI: 10.1063/1.2131191]

I. INTRODUCTION

Nonlinear, all-optical processes can be used to generate electrical currents in solids. Among such processes is a nonresonant, second-order [$\chi^{(2)}$] effect which has come to be known as optical rectification and which was observed by Bass *et al.*[1] These researchers used a ruby laser pulse to induce a time-dependent, bound-charge polarization density in several insulating crystals. Today, optical rectification is often used to generate terahertz radiation using femtosecond pulses. However, it has also been recognized that *resonant* nonlinear processes using photons with energy greater than the electronic band gap, i.e., $\hbar\omega > E_g$, can also be used to generate *free*-carrier electrical currents in semiconductors. One such process involves the generation of electrical currents in multi-quantum-well GaAs/GaAlGas (Ref. 2) or bulk GaAs (Ref. 3) via a $\chi^{(3)}$ process through the quantum interference of single- and two-photon absorption pathways for harmonically related beams. However, single-color beams can also induce shift or injection currents in noncentrosymmetric semiconductors via resonant $\chi^{(2)}$ effects.[4–13] Although the current amplitude, similar to free-carrier generation, varies linearly with the incident-beam intensity consistent with a single-photon absorption process, the generation mechanism is governed by a third-rank tensor. Nonetheless, shift and injection currents are due to different physical mechanisms and possess different crystal symmetry properties. The shift current, which has also been referred to as "above band-gap optical rectification"[7] or the "linear photovoltaic effect,"[4] is the result of a shift of the center of charge within a unit cell during optical excitation, e.g., involving transitions from valence to conduction bands. The injection current, which has also been referred to as the "circular photogalvanic effect"[4] occurs in only 18 of the 21 noncentrosymmetric crystal classes and involves the generation of a polar distribution of charge in momentum space due to interference between absorption processes induced by orthogonally polarized beams; maximal currents are produced for circularly polarized light.

The three different types of currents associated with a $\chi^{(2)}$ nonlinearity have to date been studied using disparate techniques and usually in different materials. For example, injection currents have been generated in CdSe via cw beams and observed via charge collection on electrodes,[10] while injection currents have been generated in strained GaAs. Shift and injection currents have been generated in bulk GaAs and strained GaAs quantum wells (QWs), respectively, using femtosecond pulse excitation and observed via the emitted terahertz radiation.[11,12] Here, we report on the systematic study of both shift and injection currents in CdSe and CdS ($E_g = 1.75$ eV ≡ 708 nm, and 2.50 eV ≡ 495 nm, respectively, at 295 K) using the same generation and detection techniques. The wurtzite symmetry allows both types of currents to be generated in each crystal, even simultaneously under certain conditions. The currents are generated by femtosecond optical pulses with photon energy $\hbar\omega > E_g$ and observed via the emitted terahertz radiation. The currents can be distinguished by their dependences on the optical polarization

[a]Present address: Physikalisch-Technische Bundesanstalt, Bundesallee 100, D-38116 Braunschweig, Germany.
[b]Electronic mail: vandriel@physics.utoronto.ca

and sample orientation and, in principle, by their temporal behavior. Terahertz based probing[12] allows magnitudes of the currents to be measured noninvasively, and, in principle, even time resolved, avoiding the various drawbacks of electrode-based experiments.[10] From the measured currents we are able to obtain values for the associated tensor elements that should provide tests for theoretical models of the nonlinear optical response of crystals.

The remainder of this paper is organized as follows. In the next section we briefly summarize the theoretical aspects of shift and injection current generation and evolution and offer a simple hydrodynamic model for the current dynamics. This will be followed by a description of the sample characteristics, the optical sources used to generate the currents, and the terahertz diagnostic techniques. The properties of the currents, specifically the relative magnitudes and their dependence on optical polarization and sample orientation are then given followed by a summary and conclusions.

II. THEORETICAL ASPECTS OF SHIFT AND INJECTION CURRENTS

A. Current sources

Rectification, shift, and injection currents have been described using a phenomenological model by a number of authors,[4,5] while Sipe and Shkrebtii[6] have taken a more fundamental approach to show how these currents can be understood as arising from nonlinear optical effects. They describe the current generation in the single-particle approximation approach using Fermi's golden rule and relate the macroscopic current generation process to divergent components of a second-order nonlinear susceptibility $\chi^{(2)}$.

In general, for an optical electric field defined by $\boldsymbol{E}(t)=\boldsymbol{E}(\omega)\exp(-i\omega t)+\mathrm{cc}$. excitation of a noncentrosymmetric material at two frequencies ω_1 and ω_2 leads to a second-order polarization density $\boldsymbol{P}(\omega_D)=\epsilon_0\chi^{(2)}(-\omega_D;\omega_1,-\omega_2)\boldsymbol{E}(\omega_1)\boldsymbol{E}(\omega_2)^*$ where $\omega_D=\omega_1-\omega_2$; for pulsed excitation, one sums over all ω_1 and ω_2 for constant ω_D. In the limit where $\omega_D\rightarrow 0$ (i.e., $\omega_1\rightarrow\omega_2=\omega$) for a cold, clean semiconductor the second-order susceptibility can be written as the sum of a nondivergent term and two terms with an actual physical divergence, viz.,

$$\lim_{\omega_D\rightarrow 0}\vec{\vec{\chi}}^{(2)}(-\omega_D;\omega_1,-\omega_2) = \vec{\vec{\chi}}_R^{(2)}(-\omega_D;\omega_1,-\omega_2)+\frac{\vec{\vec{\sigma}}(-\omega_D;\omega_1,-\omega_2)}{-i\omega_D}+\frac{\vec{\vec{\eta}}(-\omega_D;\omega_1,-\omega_2)}{(-i\omega_D)^2}. \quad (1)$$

Each of the three components can be related to the different current generation processes discussed above:

(i) $\vec{\vec{\chi}}_R^{(2)}$ is the *rectification* current tensor. A rectification current is established through a nonresonant process in which a bound-charge dipole oscillates in an asymmetric potential. Quantum mechanically it involves the excitation of virtual carriers for any $\hbar\omega$ (for any $\hbar\omega$ there are always pairs of valence and conduction bands with which the photons are nonresonant) and creates a polarization that follows the pulse intensity. Because of its nonresonant characteristic, for the same optical intensity a rectification current is much smaller than a shift or injection current in cases where they simultaneously occur, and will not be considered further here.

(ii) $\vec{\vec{\sigma}}$ is the *shift* current tensor and is purely real.[6] The shift current density can be written

$$\boldsymbol{J}_{\mathrm{shift}}(\omega_D)=\vec{\vec{\sigma}}(-\omega_D;\omega_1,-\omega_2):\boldsymbol{E}(\omega_1)\boldsymbol{E}^*(\omega_2). \quad (2)$$

The current, which is generated only for resonant excitation, i.e., $\hbar\omega>E_g$, arises due to the difference of the center of the electronic charge in the unit cell for valence- and conduction-band wave functions. A shift current follows the temporal profile of the optical intensity.

(iii) $\vec{\vec{\eta}}$ is the *injection* current tensor and is purely imaginary.[6] As noted earlier, the injection current occurs due to the quantum interference between absorption pathways associated with orthogonal components of the beam polarization. This leads to a polar distribution of electrons or holes in momentum space, resulting in current injection that temporally follows the optical intensity but whose decay characteristics are related to momentum scattering. From Eq. (1) the current source can be written

$$\frac{\partial\boldsymbol{J}_{\mathrm{inj}}}{\partial t}=-i\omega_D\boldsymbol{J}_{\mathrm{inj}}(\omega_D)=\vec{\vec{\eta}}(-\omega_D;\omega_1,-\omega_2):\boldsymbol{E}(\omega_1)\boldsymbol{E}^*(\omega_2), \quad (3)$$

where the factor $-i\omega_D$ corresponds to a derivative in the time domain. The tensor η_{abc} is antisymmetric in the last two Cartesian indices[6] (i.e., $\eta^{(2)}_{abc}=-\eta^{(2)}_{acb}$). For three of the 21 noncentrosymmetric crystal classes, including the zinc-blende ($\bar{4}3m$ symmetry) crystal class associated with many III-V semiconductors, η_{abc} is identically zero.

The wurtzite ($6mm$ symmetry) crystal structure is a common, hexagonal crystal structure that allows both injection and shift currents. This structure possesses three unique, nonzero $\vec{\vec{\sigma}}^{(2)}$ tensor elements, $\sigma^{(2)}_{zzz}$, $\sigma^{(2)}_{zxx}$, $\sigma^{(2)}_{xzx}=\sigma^{(2)}_{xxz}$, and one unique $\vec{\vec{\eta}}^{(2)}$ tensor elements, viz., $\eta^{(2)}_{xzx}=-\eta^{(2)}_{xxz}$ where z is taken along the hexagonal (optical) axis and x is any direction orthogonal to this axis. We chose to study two II-VI wurtzite structure semiconductors, CdSe and CdS, since their properties are well known, fundamental or second-harmonic pulses from a Ti:sapphire laser can be used to excite them, and they are commercially available. For the optical pulses used in our experiments the absorption coefficient for CdS (Refs. 14 and 15) is $\alpha=14/\mu$m at 3.0 eV (410 nm),and $\alpha=5/\mu$m at 1.80 eV (690 nm) for CdSe.[15,16] The variation of absorption coefficient with sample orientation is $<10\%$ for both materials and photon energies of interest to us.

For pulsed excitation, if $\boldsymbol{E}(t)$ is the electric field for the optical pulse, the shift and injection current components for the wurtzite structure can be written as

$$(J_{\mathrm{shift}})_z=2\sigma_{zzz}|E_z|^2+2\sigma_{zxx}|E_x|^2, \quad (4)$$

$$(J_{\mathrm{shift}})_x=4\sigma_{xzx}|E_x||E_z|\cos(\phi^z-\phi^x), \quad (5)$$

and

$$(\partial/\partial t)(J_{\mathrm{inj}})_x = -4i\eta_{xzx}|E_x||E_z|\sin(\phi^z-\phi^x), \tag{6}$$

where $\phi^z-\phi^x$ is the relative phase of the optical field components polarized along the x and z directions. The maximum injection current occurs for circularly polarized light. For light with both x and z polarization components, shift and injection currents can be generated simultaneously, albeit along different crystallographic directions allowing them to be distinguished. Given the selection rules for optical transitions, if the incident light is circularly polarized the injection current can be spin polarized; however, the spin properties of the current are not considered here.

In the case of the shift current, optical excitation induces a shift in the center of charge, $\boldsymbol{r}_{\mathrm{shift}}$, given by

$$\boldsymbol{J}_{\mathrm{shift}} = \frac{e\alpha I_p}{\hbar\omega}\boldsymbol{r}_{\mathrm{shift}}, \tag{7}$$

where I_p is the local pump intensity. The shift current and vector displacement are associated entirely with electron displacement and exist only while the material is illuminated; there is no shift for holes in the lattice reference frame. Equation (7) can be used with Eqs. (4) and (5) to deduce a shift distance from a measured shift current density.

In the case of injection current where electrons (holes) are created with an effective group speed, $\boldsymbol{u}_e^0$ ($\boldsymbol{u}_h^0$), the injected current density can be written as

$$\frac{\partial \boldsymbol{J}_{\mathrm{inj}}}{\partial t} = \frac{e\alpha I_p}{\hbar\omega}(\boldsymbol{u}_h^0-\boldsymbol{u}_e^0). \tag{8}$$

From conservation of energy and momentum in the optical excitation process one has $\boldsymbol{u}_e^0=-m_h^*/m_e^*\boldsymbol{u}_h^0$ where $m_{e,h}^*$ are the effective masses of electrons and holes. For a measured injection current, from Eq. (8) one can then deduce the average injection velocities of electrons and holes. Because the effective mass of holes is much larger than that of electrons (see below) nearly all the injection current is associated with electron motion.

B. Current evolution

The macroscopic current dynamics for shift and injection currents involve not only the generation process but also the subsequent evolution of the charge distributions in the sample. To gain insight into the dynamics we employ a simple hydrodynamic model in which electrons (holes) are taken to move with average velocity $\boldsymbol{u}_e$ ($\boldsymbol{u}_h$). On a time scale short compared to the carrier recombination time ($\gg$picoseconds in our samples), the evolution of the electron (hole) density, $N_e(N_h)$, is governed by

$$\frac{\partial N_e}{\partial t} + \boldsymbol{\nabla}\cdot(N_e\boldsymbol{u}_e) = \left.\frac{\partial N_e}{\partial t}\right|_{\mathrm{source}}, \tag{9}$$

where the source term is given by $\partial N_e/\partial t|_{\mathrm{source}}=\alpha I_p(\boldsymbol{r}-\boldsymbol{r}_{\mathrm{shift}})/\hbar\omega$ and $\boldsymbol{r}_{\mathrm{shift}}$ is obtained from Eq. (7). A similar equation exists for the hole density, although as noted above, there is no shift in the source term. The total current at any time is $\boldsymbol{J}=\boldsymbol{J}_h+\boldsymbol{J}_e+\boldsymbol{J}_{\mathrm{shift}}=e(N_h\boldsymbol{u}_h-N_e\boldsymbol{u}_e)+\boldsymbol{J}_{\mathrm{shift}}$ where the electron velocity evolution is governed by

$$\frac{\partial \boldsymbol{u}_e}{\partial t} + (\boldsymbol{u}_e\cdot\boldsymbol{\nabla})\boldsymbol{u}_e + \frac{\boldsymbol{\nabla}(N_eT)}{m_e^*N} = \frac{-e\boldsymbol{E}}{m_e^*} - \frac{\boldsymbol{u}_e}{\tau_m} + \frac{(\boldsymbol{u}_e^0-\boldsymbol{u}_e)}{N_e}\left.\frac{\partial N_e}{\partial t}\right|_{\mathrm{source}}, \tag{10}$$

with a similar equation determining $\boldsymbol{u}_h$. Here T is the common electron/hole temperature, τ_m is the electron momentum relaxation time due to phonon- or carrier-induced scattering processes, and $\vec{E}$ is an electric field that arises from charge density imbalance $e(N_h-N_e)$ and from $\boldsymbol{J}$. The space-charge and current sources produce scalar (Φ) and vector potentials ($\boldsymbol{A}$) which can be calculated using Green function techniques[17] for the appropriate boundary conditions; the electric field is then given by $\boldsymbol{E}=-\boldsymbol{\nabla}\Phi-\partial\boldsymbol{A}/\partial t$. For our experiments where the illuminated spot sizes are $W\sim 100$ μm full width at half maximum (FWHM) in diameter and the relative dielectric constants[15] are $\epsilon=9.3$ (8.7) for CdSe (CdS), respectively; the time scales ($\sim$100 fs) for current evolution are $<W\sqrt{\epsilon}/c$ therefore the electrostatic approximation is inappropriate; and the electric field arises mainly from current sources through $\boldsymbol{A}$ if one uses the Coulomb gauge.

The momentum relaxation time in CdSe (CdS) can be estimated from the room-temperature mobility[15] of 600 (300) $\mathrm{cm^2V^{-1}\,s^{-1}}$ for electrons and 15 (10) $\mathrm{cm^2V^{-1}\,s^{-1}}$ for holes with $m_e^*=0.12m_0$ ($0.21m_0$) and $m_h^*=0.45m_0$ ($0.7m_0$). One obtains $\tau_m=40$ fs (36 fs) for CdSe (CdS). For holes the corresponding relaxation times are $\sim$3 fs for both materials. Assuming that electrons and holes are rapidly thermalized among themselves on a time scale of the order of τ_m, the carrier temperature following thermalization for Boltzmann statistics is $(\hbar\omega-E_g)/3k_B$ where k_B is Boltzmann's constant. The temperature is spatially uniform over the illumination region and decays to the lattice temperature on a 200 fs time scale.[17]

Equations (9) and (10) can be solved for the total current density $\boldsymbol{J}$ using standard numerical techniques. From the temporally and spatially dependent current density, the total radiated terahertz field can be calculated and related to the field at an electro-optic crystal (see below) using a simple propagation code.[18] For the optical pulse widths and peak powers used in the experiments the injected carrier densities are typically $<10^{18}$ $\mathrm{cm^{-3}}$ and one finds that the current evolution is dominated by the generation terms, momentum scattering, and, to a lesser extent, diffusion. Only at much higher injected carrier densities do significant currents arise from fields induced by space charge or the initially currents themselves; in such a case the total current no longer varies linearly with the optical intensity. If τ_m is much smaller than the optical pulse width, the injection current follows the optical pulse envelope and the injection current has a temporal behavior similar to a shift current with an effective shift current tensor amplitude of $-i\eta\tau_m$. Figure 1 shows the evolution of the area charge density following current injection in the surface region of CdS for a 0.3 nJ ($I_p\sim 5$ $\mathrm{MW\,cm^{-2}}$), 410 nm Gaussian temporal and spatial pulse focused to a spot diameter of 100 μm with $u_e^0=20$ $\mathrm{km\,s^{-1}}$ and $\tau_m=40$ fs. It is interesting to note that the charge density is effectively distributed as the derivative of a Gaussian function as ex-

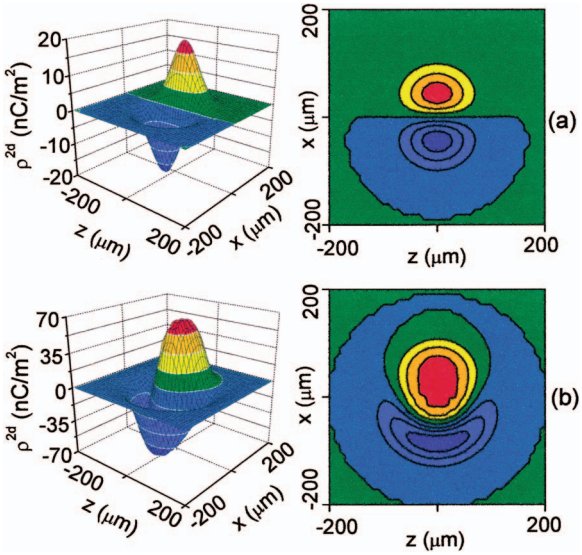

FIG. 1. (Color) (a) Simulated area charge density (i.e., volume charge density integrated over excitation depth) at $t=0$ (peak of excitation pulse) for injection current excitation in CdS with parameters given in text. The same information is displayed as a surface plot and a contour plot. (b) Area charge density at $t=35$ ps.

pected from the continuity equation. After a time as long as 35 ps the surface density has hardly evolved although the spatial pattern shows an interesting asymmetric pattern in the direction of the initial current; because of the low carrier mobility charge relaxation is slow, the electric field driven current is small, and virtually no terahertz radiation is generated by field-driven currents following the initial current injection. Figure 2(a) displays typical simulated total currents associated with shift and injection current sources for a 60 fs optical pulse width and 10^{17} cm^{-3} peak carrier density; values of τ_m between 10 and 200 fs were chosen to illustrate how the currents vary with time. Figure 2(b) shows the corresponding terahertz radiation generated by the current sources depicted in Fig. 2(a). For the largest momentum relaxation a large phase difference occurs between the terahertz signatures of the shift and injection current, while a short momentum relaxation time results in a small phase difference. Some of the temporal characteristics of the terahertz fields shown in Fig. 2(b) reflect propagation aspects.

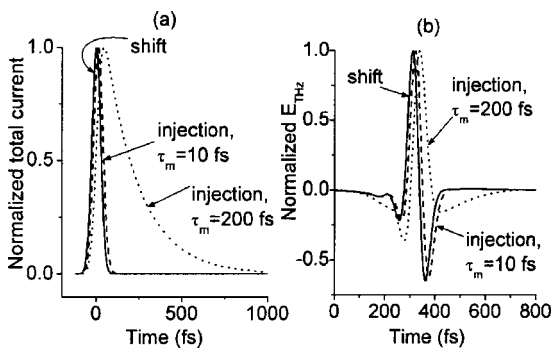

FIG. 2. (a) Calculated normalized total current for shift and injection current sources in CdS with 10 and 200 fs electron momentum scattering time for an incident 60 fs optical pulse. (b) The corresponding terahertz electric fields.

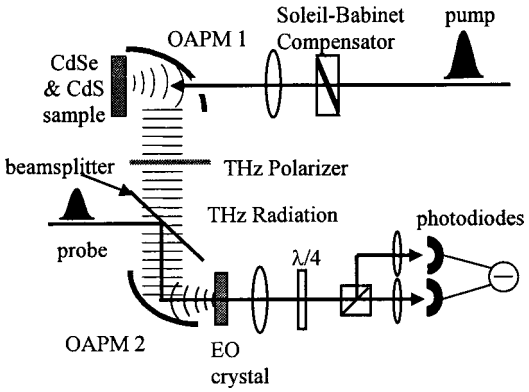

FIG. 3. Apparatus for recording terahertz radiation generated by induced currents in CdSe; the OAPM are off-axis parabolic mirrors.

In discussing shift and injection currents it is appropriate to offer some figures of merit for the effectiveness of the nonlinear processes in generating currents. Because shift current involves an alteration of the center of negative charge within a unit cell a measure of the effectiveness of the shift current generation process is the fraction of the bond length (upper limit) that the charge shifts. The effectiveness of the injection current process is taken to be the ratio of the average injected (and directed) velocity of the electrons divided by the (undirected) group velocity the electrons have when excited by a photon of the same energy.

III. EXPERIMENTAL METHODOLOGY

Figure 3 shows the experimental setup used to generate and detect shift and injection currents in CdS and CdSe. Two different Kerr lens mode-locked Ti:sapphire lasers were used as optical sources. The first is a Coherent Mira laser which was mainly used for the CdSe experiments. For these experiments, the center wavelength was tuned between $690<\lambda<730$ nm, producing pulses at a 76 MHz repetition rate with a pulse width between 200 and 300 fs and a peak power between 1.7 and 7.4 kW. A homebuilt Ti:sapphire laser was used to generate 60 fs, 820 nm pump pulses at an 80 MHz repetition rate and with a peak power of 120 kW. The 820 nm output pulses were frequency doubled with a 1-mm-thick type I beta-barium borate (BBO) crystal to produce 410 nm, pulses with a peak power of 6 kW. The pulse width was measured to be 60 fs via parametric mixing of the 410 and 820 nm pulses in a 160-μm-thick BBO crystal. The 410 nm pulses were used for the CdS experiments.

For the CdSe experiments, the polarization of the pump pulse was controlled by a Soleil-Babinet compensator and the pulse was focused at normal incidence onto the sample with a spot diameter (FWHM) of $W\sim 130$ μm, producing a peak carrier density $<10^{18}$ cm^{-3}. An induced current generated terahertz radiation which was collected by an off-axis Al parabolic mirror that has both a diameter and a focal length of 5 cm. The optical beam passed through a 3-mm-diameter hole in the mirror. The terahertz radiation passed through a wire grid polarizer, was subsequently refocused with a second, identical, off-axis parabolic mirror (OAPM) (labeled OAPM 2 in Fig. 3), and was measured via free-space electro-optic (EO) sampling. An optical probe pulse

was obtained from the laser output and combined with the terahertz beam via a silicon-on-sapphire beam splitter. These beams were spatially overlapped on an EO crystal with the temporal overlap controlled by a delay stage. The terahertz beam induced a polarization change in the probe pulse and the differential intensity in the probe beam, $\Delta I/I$, was measured using a balanced detector. For the CdSe experiments a 500-μm-thick ZnTe EO crystal was used with $\sim$250 fs, $\sim$700 nm probe pulses resulting in a bandwidth of$<$2 THz.

For the CdS experiments the polarization of the 410 nm, 60 fs pump pulse was controlled by a superachromatic waveplate rather than the Soleil-Babinet compensator since the latter stretches the pulses temporally by 50%. Experiments were performed both with and without a pump focusing lens, resulting in a spot diameter at the sample of $W\sim 100$ μm or 1.4 mm, respectively, and peak carrier densities of 9×10^{17} and 5×10^{15} cm^{-3}. In order to improve the alignment of the probe and the terahertz radiation on the EO crystal, the beam splitter was removed and the probe pulse was focused onto the EO crystal through a 3-mm-diameter hole in the off-axis parabolic mirror. For the CdS experiments, besides the ZnTe EO crystal a 120-μm-thick GaP crystal was used to achieve a larger detection bandwidth of $\sim$3 THz when used with 820 nm, 60 fs probe pulses.

Several CdSe and one CdS single crystals with dimensions $\sim 1\times 1$ cm^2 by 1 mm were obtained from Cleveland Crystals and cut with their optic axis in the plane of the largest surface (*a* plate). This was necessary for experiments conducted with normally incident beams since the σ_{xxx} shift and η_{xxx} injection tensor elements vanish for the wurtzite structure, and one requires the current or a component of the optical field to be polarized along the optic axis to generate nonzero currents. In what follows we take the *x* axis to be in the plane of the sample with the *y* axis pointing into the sample. Samples were mechanically polished and, in some cases, etched. There was insignificant dependence of the observed signals on surface preparation, except as noted below.

IV. RESULTS AND DISCUSSION

A. Shift and injection currents in CdSe

In the first set of experiments, shift currents were generated in the CdSe samples for linear- and circular-polarized optical pulses with a fixed wavelength of 706 nm. The solid and dashed line of Fig. 4 show two EO traces of the terahertz response for an optical beam linearly polarized, and currents directed along the optic axis, i.e., making use of the allowed σ_{zzz} tensor element. For the two traces the sample was reoriented in its plane by 180° and, as expected, the current and terahertz signal display a 180° phase shift. The dotted and dashed-dotted curves of Fig. 4 show two EO traces corresponding to excitation of the sample with an optical beam polarized along the *x* axis. No measurable signal is observed, consistent with σ_{xxx} expected to be zero by symmetry.

Typical EO curves for the terahertz radiation produced by the injection current are shown in Fig. 5. The 706 nm pump pulse was circularly polarized and the *x* component of the terahertz radiation was detected making the experiments sensitive to the η_{xzx} tensor element. As expected, the terahertz trace changes sign when the polarization is changed from left- to right-handed circularly polarized, corresponding to a reversal in the current direction. As shown in the inset to Fig. 5 the terahertz radiation amplitude varies linearly with optical pump intensity consistent with results from our simulations and indicating that space-charge effects, *inter alia*, do not significantly influence the current amplitude at our carrier densities ($<10^{18}$ cm^{-3}). The shift and injection currents were also measured for $\lambda>700$ nm pulses; the terahertz (current) amplitude became immeasurable as expected when $\hbar\omega<E_g$.

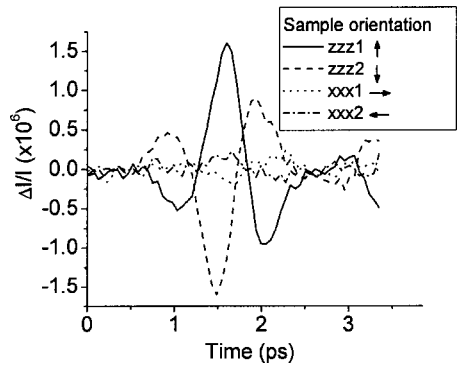

FIG. 4. EO traces of terahertz radiation for the shift current excited in CdSe by $\sim$210 fs linearly polarized pulses at 706 nm with peak intensity of 17 MW cm^{-2}. The vertical arrows in the legend indicate that the beam is polarized along the optic (*z*) axis with the current making use of the σ_{zzz} tensor element; the horizontal arrows indicate that the beam is polarized perpendicular to the optic axis, with the terahertz trace sensitive to any σ_{xxx} tensor. Flipping of arrows indicates reorientation of the sample by 180°.

The current dynamics and terahertz propagation model[18] were used to extract the magnitude of the σ_{zzz} and η_{zxz} tensor elements from the measured EO signal, $\Delta I/I$. In practice these parameters were varied in the calculation until they yielded EO terahertz traces similar to the ones observed experimentally. From the simulations the terahertz peak amplitude varied nearly linearly with the magnitude of the tensor element. The shape of the EO traces is dictated by aspects of the terahertz propagation and detector parameters, especially bandwidth. While the temporal behavior of the currents cannot be extracted from the experimental data, one can determine the current magnitude, corresponding to different opti-

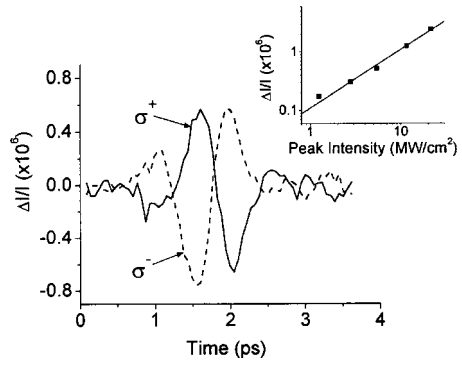

FIG. 5. EO traces of terahertz radiation produced by injection current excited in CdSe by $\sim$210 fs, 706 nm pulses with a peak intensity of 17 MW cm^{-2} and for oppositely handed circular polarizations. The inset shows the intensity dependence of the EO signal (dots) with the solid line indicating linear behavior.

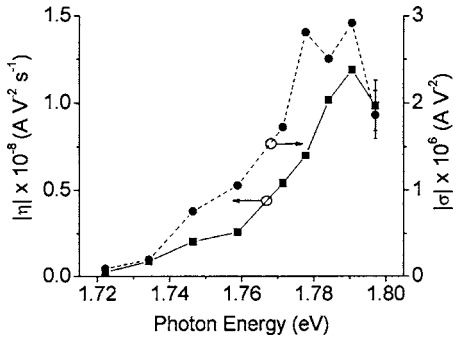

FIG. 6. Magnitude of σ_{zzz} and η_{xzx} in CdSe as function of photon energy (solid dots and squares, respectively); the solid and dashed lines are guides to the eye.

cal pumping conditions. The values of the σ_{zzz} and σ_{xzx} tensor elements are shown in Fig. 6 as a function of $\hbar\omega$. In general, the derived values of both tensor elements increase monotonically with $\hbar\omega$ but peak or reach a plateau for photon energies above 1.78 eV. For $\hbar\omega=1.80$ eV, $\sigma_{zzz}=1.5\times10^{-6}$ A V^{-2} while $\eta_{xzx}=i1.5\times10^{8}$ A V^{-2} s^{-1}, assuming $\tau_m=40$ fs (as determined from mobility). The actual momentum scattering time for electrons excited with energies greater than the room-temperature kinetic energy of 25 meV could be shorter making η_{xzx} larger than the value quoted. The peak current densities obtained from the simulations are 5 and 8 kA cm^{-2} for shift and injection current, respectively, for a peak intensity of 10 MW cm^{-2} at $\hbar\omega=1.80$ eV. For CdSe the bond distance, which as noted above represents the maximum shift distance, is 0.25 nm.[19] From the measurement of σ_{zzz} at 1.80 eV for CdSe we deduce a shift distance of 0.1 nm or 40% of the bond length. We have also carried out measurements for other incident optical polarizations to determine the magnitude of σ_{xzx} and σ_{zxx}; the results are summarized in Table I. All experimentally derived values are considered accurate to within 40%, mainly determined by the collection efficiency aspects of terahertz radiation.

The temporal resolution of the above experiments was limited by the 240 fs pulse width. In an attempt to improve the temporal resolution, experiments were conducted with 410 nm, 60 fs pulses. Unfortunately, optical polarization-insensitive terahertz signals were produced that were much larger than those associated with shift or injection currents, making signal extraction difficult. These larger signals are likely related to the small absorption depth (<50 nm) making Dember field or surface-related effects more prominent. For these reasons, the terahertz signal due to the shift and injection current could not be isolated.

TABLE I. Summary of results for CdSe and CdS.

Property	CdSe (@ 690 nm)	CdS (@ 410 nm)
σ_{zzz}	1.5×10^{-6} A V^{-2}	8×10^{-6} A V^{-2}
σ_{zxx}	$\sim0.5\times10^{-6}$ A V^{-2}	$\sim3\times10^{-6}$ A V^{-2}
σ_{xzx}	$<1\times10^{-7}$ A V^{-2}	$<8\times10^{-7}$ A V^{-2}
Peak shift current	5 kA cm^{-2} (10 MW cm^{-2}) for σ_{zzz}	50 kA cm^{-2} (75 MW cm^{-2}) for σ_{zzz}
Shift distance	0.1 nm	0.2 nm
η_{xxz}	$i1.5\times10^{8}$ A V^{-2} s^{-1}	$i4\times10^{8}$ A V^{-2} s^{-1}
Peak injection current	8 kA cm^{-2} (10 MW cm^{-2})	80 kA/cm^{2} (75 MW cm^{-2})
Electron injection speed	9 km s^{-1}	20 km s^{-1}
Injection current efficacy	3%	2%

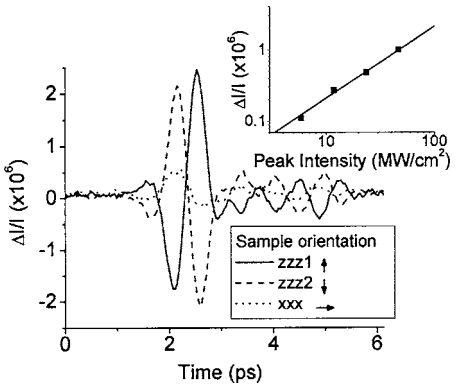

FIG. 7. EO traces of terahertz radiation corresponding to the shift current excited in CdS by a 60 fs optical pulse with $\hbar\omega=3.0$ eV and a peak intensity of 75 MW cm^{-2} for different sample orientations. The arrows in the legend correspond to sample orientation (see Fig. 1 for explanation). The inset shows the measured intensity dependence of terahertz amplitude (solids dots); the solid line corresponds to linear dependence.

B. Shift and injection currents in CdS

Signatures of shift and injection currents were obtained in CdS using 410 nm, 60 fs pulse excitation. However, as with the CdSe experiments conducted at 410 nm experiments were complicated by the generation of terahertz radiation not related to shift or injection currents. As with the CdSe experiments this may be related to the small, 90 nm absorption depth. However, the surface contribution to the terahertz signal in CdS is experimentally much less than the corresponding signal in CdSe and can be minimized through adjustment of optical excitation and detection geometry. Figure 7 shows CdS EO terahertz traces recorded with the 500-μm-thick ZnTe crystal corresponding to the σ_{zzz} shift current tensor element for sample orientations that differ by 180°. Also shown are terahertz traces from experiments that might detect a σ_{xxx} element. Somewhat surprisingly there was a small signal. Since theoretically the σ_{xxx} tensor element is expected to be zero, the signal likely arises from induced surface fields. Similarly, the small difference in amplitudes of terahertz traces for experiments sensitive to the σ_{zzz} tensor element are also related to surface field. Figure 8 shows the EO terahertz traces from experiments sensitive to the η_{xzx} injection current tensor element. The terahertz traces associated with both the σ_{zzz} and η_{xzx} tensor elements inverted when the sample was rotated in plane by 180°. Furthermore, the signal due to the injection current inverted when the pump polarization was changed from left- to right-handed circularly polarized, confirming the symmetry properties of the shift and injection currents.

For both shift and injection currents, the shape of the EO terahertz traces do not measurably change with pump intensity and the insets of Figs. 7 and 8 show that for both currents the terahertz amplitude varies linearly with pump intensity as expected. Using the current generation and terahertz propagation model described above, the magnitude of the

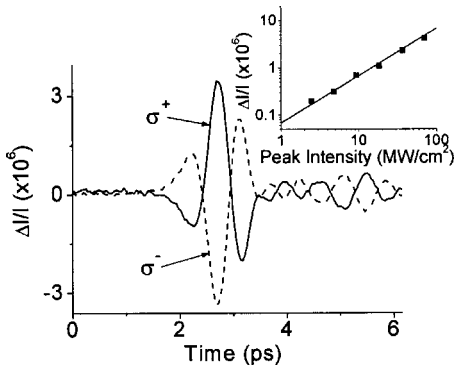

FIG. 8. EO traces of terahertz signal corresponding to the injection current excited in CdS by a 410 nm, 60 fs optical pulse with a peak intensity of 75 MW cm^{-2} for different circular polarizations. The inset shows an intensity study with the solid line corresponding to linear dependence.

peak shift current for optical fields polarized along, and currents directed along the optical axis, was determined to be 50 kA cm^{-2} for an intensity of 75 MW cm^{-2}. This corresponds to $\sigma_{zzz}=8\times10^{-6}$ A V^{-2}. Similarly, the peak injection current density for the same peak intensity is 80 kA cm^{-2}. Assuming a momentum scattering time of 40 fs, $\eta_{xzx}=i4\times10^{8}$ A V^{-2} s^{-1}. For CdS the bond distance is 0.26 nm.[19] From the measurement of σ_{zzz} at 1.80 eV for CdS we deduce a shift distance of 0.2 nm or 80% of the bond length.[19] Experiments were also conducted to detect terahertz radiation associated with σ_{xzx} and σ_{zxx}. The values of these elements as well as a summary of all our measurements are indicated in Table I.

Theoretically, the injection current decay is influenced by the momentum scattering time while the shift current follows the optical pulse intensity. In an attempt to observe this difference the EO terahertz traces for shift and injection currents and the corresponding terahertz spectra were measured with the 120 μm GaP EO crystal. These are shown in Fig. 9; no phase shift was observed. The measured terahertz bandwidth of 3 THz (half maximum) is considerably smaller than the theoretical bandwidth of 7 THz given the optical pulse width and the dispersion of GaP.[13] Given the experimental temporal resolution, the signal-to-noise ratio, and no measurable phase shift, an upper bound of the momentum scattering time can be estimated to be <100 fs, consistent with the time derived from mobility measurements[15] as well as measurements of the energy relaxation time.[17] We attempted to increase the momentum scattering time by mounting the sample in a cryostat and decreasing the temperature to 81 K. Electron-hole scattering was reduced by increasing the excitation spot diameter (FWHM) to 1.4 mm, yielding a peak carrier density of only 5×10^{15} cm^{-3}. However, no detectable phase difference between the shift and injection current terahertz traces could be observed, although the amplitude of the signal increased by $\sim$50% when the temperature was reduced. The lack of change may reflect the fact that the electrons have a large (320 meV) kinetic energy, so while phonon absorption is strongly suppressed, even at low temperatures phonon emission is only slightly suppressed. Electron scattering in the near surface region states is likely an additional momentum scattering mechanism, which is enhanced by the short absorption depth.

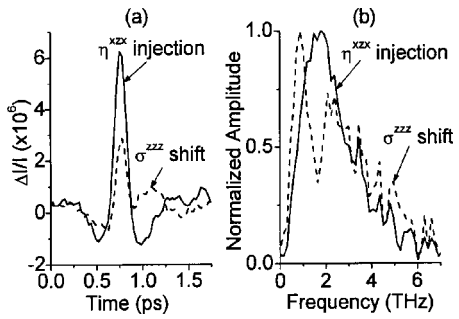

FIG. 9. (a) EO traces of terahertz signal for injection and shift currents in CdS using the 120-μm-thick GaP EO crystal. (b) The corresponding terahertz spectra.

V. SUMMARY

We have carried out a systematic comparison of shift and injection currents induced in CdSe and CdS by femtosecond optical pulses and detected through the emitted terahertz radiation. In all cases the terahertz radiation and the currents displayed the expected dependence on optical polarization and sample orientation, consistent with the symmetry properties of the shift and injection current tensors. The terahertz signals varied linearly with optical intensity, consistent with the theory. There was no evidence of space-charge-related currents for injected carrier densities up to 10^{18} cm^{-3}. Values for the key parameters associated with shift and injection currents have been measured for both CdSe and CdS and are summarized in Table I. No temporal difference between the EO terahertz traces from shift and injection currents in CdS were measured, implying the momentum scattering time in all experiments is <100 fs.

ACKNOWLEDGMENTS

The authors thank John Sipe and members of his research group for useful discussions. Financial support from Photonics Research Ontario and the Sciences and Engineering Research Council of Canada is greatly appreciated.

[1] M. Bass, P. A. Franken, J. F. Ward, and G. Weinreich, Phys. Rev. Lett. **9**, 446 (1962).
[2] E. Dupont, P. B. Corkum, H. C. Liu, M. Buchanan, and Z. R. Wasilewski, Phys. Rev. Lett. **74**, 3596 (1995).
[3] A. Haché, Y. Kostoulas, R. Atanasov, J. L. P. Hughes, J. E. Sipe, and H. M. van Driel, Phys. Rev. Lett. **78**, 306 (1997).
[4] E. L. Ivchenko and G. E. Pikus, JETP Lett. **27**, 604 (1978).
[5] B. I. Sturman and V. M. Fridkin, *The Photovoltaic and Photorefractive Effects in Noncentrosymmetric Materials* (Gordon and Breach Science, Philadelphia, 1992).
[6] J. E. Sipe and A. I. Shkrebtii, Phys. Rev. B **61**, 5337 (2000).
[7] J. B. Khurgin, J. Opt. Soc. Am. B **11**, 2492 (1994).
[8] R. von Baltz and W. Kraut, Phys. Rev. B **23**, 5590 (1981); V. I. Belinicher, Phys. Lett. **66A**, 213 (1978).
[9] S. D. Ganichev and W. Prettl, J. Phys.: Condens. Matter **15**, R935 (2003); S. D. Ganichev, E. L. Ivchenko, S. N. Danilov, J. Eroms, W. Wegscheider, D. Weiss, and W. Prettl, Phys. Rev. Lett. **86**, 4358 (2001).
[10] N. Laman, A. I. Shkrebtii, J. E. Sipe, and H. M. van Driel, Appl. Phys. Lett. **75**, 2581 (1999).
[11] M. Bieler, N. Laman, H. M. van Driel, and A. L. Smirl, Appl. Phys. Lett. **86**, 061102 (2005).
[12] D. Côté, N. Laman, and H. M. van Driel, Appl. Phys. Lett. **80**, 905 (2002).

[13]Q. Wu and X.-C. Zhang, Appl. Phys. Lett. **70**, 1784 (1997).
[14]S. Ninmiya and S. Adachi, J. Appl. Phys. **78**, 1183 (1995).
[15]*Semiconductors-Basic Data*, 2nd ed., edited by O. Madelung (Springer, Berlin, 1996).
[16]M. Schäffner, X. Bao, and A. Penzkofer, Appl. Opt. **31**, 4546 (1992).
[17]V. Klimov, P. Haring Bolivar, and H. Kurz, Phys. Rev. B **52**, 4728 (1995).
[18]D. Côté, J. E. Sipe, and H. M. van Driel, J. Opt. Soc. Am. B **20**, 1374 (2003).
[19]L. C. L. Y. Voon, M. Willatzen, M. Cardona, and N. E. Christensen, Phys. Rev. B **53**, 10703 (1996).